DOI: 10.21062/mft.2025.070 http://www.journalmt.com

Mechanical Alloying, an Innovative Way of Zinc Preparation for Biomaterial Applications

David Nečas (0000-0001-7731-8453), Jan Blažek (0009-0007-0646-4737), Jan Pokorný (0009-0000-8583-3893), Anna Boukalová (0009-0008-9035-4182), Jiří Kubásek (0000-0001-6008-0127)
Faculty of Chemistry and Technology, University of Chemistry and Technology in Prague. Technická 5, 160 00 Prague. Czech Republic. E-mail: necasd@vscht.cz

In this study, binary zinc-based alloys (Zn–1Mg, Zn–1Li, Zn–2Mn, wt.%) were synthesized by performing mechanical alloying (MA) of elemental powders, followed by consolidation using spark plasma sintering (SPS). The processing parameters were optimized to obtain homogeneous powders with controlled particle size. X-ray diffraction and SEM analyses confirmed the presence of secondary intermetallic phases (Mg_2Zn_{11}, $Zn_{13}Mn$, $ZnLi_2$ phases) formed during milling, which were preserved after SPS. Microstructural examination revealed a fine-grained microstructure with residual oxide networks originating from powder surfaces. Mechanical testing demonstrated significant strengthening effects after Mg and Li additions, with Zn–1Mg alloy reaching the highest hardness (128 HV1) and compressive strength (526.7 MPa), attributed to uniformly distributed Mg_2Zn_{11} precipitates. However, this strengthening was accompanied by reduced ductility. Zn–1Li exhibited the most balanced combination of strength and plasticity, while Zn–2Mn provided only a limited improvement over pure zinc. These results confirm that mechanical alloying combined with SPS is a promising route for developing biodegradable Zn-based biomaterials with enhanced properties.

Keywords: Biodegradable Metals, Zinc Alloys, Powder Metallurgy, Microstructure, Compressive Test

1 Introduction

In this work, the possibility of preparing Zn-based binary alloys from high-purity elemental powders was investigated using mechanical alloying (MA), followed by densification via spark plasma sintering (SPS). Magnesium is considered one of the most favourable alloying elements for zinc due to its excellent biocompatibility and significant strengthening effect, which is attributed to the formation of intermetallic phases with zinc. The maximum solubility of Mg in Zn is approximately 1 wt.% at the eutectic temperature, but it decreases to nearly zero at ambient conditions. Based on previous studies, the Mg content was therefore fixed at 1 wt. % in order to achieve an optimal balance between strength and plasticity [1-3]. Lithium represents another promising alloying addition for zinc-based materials in biomedical applications. It is biocompatible and has demonstrated therapeutic potential in the treatment of several conditions, including brain injury, stroke, Alzheimer's disease, and Huntington's disease [4, 5]. Manganese, an essential element in the human body, has been reported to facilitate cellular processes associated with bone metabolism and healing.

This property is particularly advantageous for biodegradable implants designed to promote osteogenesis and integration with surrounding tissues [6]. Due to the higher solubility of manganese in the zinc matrix (0.8 wt.% at 405 °C [7, 8]), the concentration was increased to 2 wt.%. Improvements in the mechanical and corrosion behaviour of Zn alloys are expected to arise primarily from precipitation strengthening due to secondary phases (e.g., Mg_2Zn_{11} [9, 10], $LiZn_4$ [11], $Zn_{13}Mn$ [8, 11]), combined with solid-solution strengthening, which is strongly influenced by the solubility limits of the individual alloying elements.

MA was employed to produce a homogeneous, fine-grained microstructure consisting of solid solutions and metastable intermetallic compounds. The resulting powders were subsequently consolidated by SPS, enabling rapid densification while suppressing grain growth [12-15].

2 Materials and methods

2.1 Material processing

In this study, Zn–1Mg (wt.%), Zn–1Li (wt.%), and Zn–2Mn (wt.%) were prepared by MA using pure metals. Input materials were in the form of powder for pure zinc powder (99.9 %, particle size <149 μm, Thermo Fisher Scientific), pure magnesium (99.8 %, particle size <44 μm, Alfa Aesar), and manganese (99.3 %, particle size <44 μm, Thermo Fisher Scientific). Lithium was added in the form of bulk pieces (0.125 cm^3). To prevent the agglomeration of powder particles during milling, 0.03 g of stearic acid was added to all selected compositions.

Based on process optimization performed on the Zn–1Mg alloy, a milling time of 4 h was selected. For Zn–1Li, the milling was carried out in two stages to break down the bulk lithium: 2 h using 15 mm milling balls, followed by 2 h with 10 mm milling balls. In both stages, the same amount of stearic acid (0.03 g) was used to minimize the sticking of powders to the milling vessel. The total weight of each powder batch was 30 g. Milling was conducted in ZrO_2 vessels under an argon atmosphere (99.95% purity) using a Retsch E-Max mill operated at 800 rpm in reverse rotation mode, with direction changes every 10 min. A water-cooling system maintained the process temperature between 30 and 50 °C. ZrO_2 balls were used with a ball-to-powder weight ratio of 10:1. The specific milling parameters for each alloy composition are summarized in Tab. 1.

The MA powders were consolidated via spark plasma sintering (SPS) using an FCT System HP-D 10 under an argon atmosphere (99.95% purity). Consolidation was carried out at 300 °C under a uniaxial pressure of 48 or 80 MPa for 10 min, using a graphite die. The heating rate was set to 100 K/min. For comparison, pure zinc powder was also sintered under the same conditions. The sintered compacts had a cylindrical shape with a diameter of 20 mm.

The alloy designations used throughout this work and the corresponding processing parameters are provided in Tab. 1. The milling conditions were chosen to obtain powders with a fine-grained microstructure, controlled particle size, low contamination, and a reduced fraction of intermetallic phases. SPS parameters were selected in line with previous studies to achieve dense, homogeneous compacts [16, 17].

Tab. 1 *Designation of studied materials according to their processing conditions*

Marking	Chemical composition	Mechanical alloying	SPS
Zn–1Mg	Zn, 1 wt.% Mg	800 RPM, 4 h, 1 mm	300 °C, 80 MPa
Zn–1Li	Zn, 1 wt.% Li	800 RPM, 2+2 h, 1 + 1.5 mm	300 °C, 48 MPa
Zn–2Mn	Zn, 2 wt.% Mn	800 RPM, 4 h, 1 mm	300 °C, 80 MPa

2.2 Phase and microstructure analyses

The prepared powders and bulk samples were analyzed using diffraction and microscopy methods. Phase composition was determined by X-ray diffraction (XRD, PANalytical X'Pert^3 Powder, Bragg–Brentano geometry, Cu Kα radiation, λ = 1.5418 Å, 40 kV, 30 mA). Optimization of MA parameters was performed by particle size distribution analysis using laser diffraction (Malvern Mastersizer 3000), and the median particle size (D_{50}) is reported. Chemical composition was verified using atomic absorption spectroscopy (AAS, Agilent 280FS AA, flame atomization).

Microstructural characterization was carried out using optical microscopy (Olympus PME3) and scanning electron microscopy (SEM, TESCAN VEGA 3 LMU) equipped with an energy-dispersive X-ray (EDX) analyzer (Oxford Instruments AZtec). Prior to observation, samples were ground with SiC papers (grit sizes P400–P2500) and polished with diamond paste (2 μm, UR-diamant) and Eposil Non-Dry suspension.

2.3 Mechanical properties

Mechanical properties were evaluated through microhardness and compression testing. Vickers microhardness (HV1) was measured using a FutureTech FM-100 tester under a load of 1 kgf. At least ten indentations were made for each condition, and average values were reported. Compression tests were performed on three specimens ($3 \times 3 \times 5$ mm^3) using an Instron 5882 testing machine at a crosshead speed of 1 mm/min at room temperature. Statistical evaluation was conducted from the collected data.

3 Results and discussion

3.1 Optimization of mechanical alloying parameters

MA is a complex process governed by two competing mechanisms: cold welding and particle fracture. The balance between these mechanisms is strongly influenced by the milling parameters, with milling time being the most critical factor (Tab. 2). Other parameters were optimized based on our previous studies [16].

Results of the particle size distribution in Table 2 show that at the initial stage of milling, cold welding dominates, resulting in the formation of coarse agglomerates and a significant increase in particle size compared to the starting powders. The maximum particle size (395 μm) was reached after 30 minutes of milling. After 1 hour, the process shifts, with particle fracture prevailing over cold welding. This transition is typically associated with the precipitation of hard and brittle intermetallic phases, which are readily fragmented under milling impacts. The finest particle size (69.3 μm) was obtained after 2 hours of milling. Further extension of milling time did not lead to additional refinement. Instead, a slight increase in particle size was observed, suggesting secondary agglomeration. This phenomenon can be explained by the progressive refinement of intermetallic phases and the dissolution of alloying elements into the zinc matrix, which decreases the extent of particle fracture during milling.

Tab. 2 *Changes in particle size distribution [μm] with different times of MA for various milling equipment*

Parameters	Milling time [hours]					
	0.18	**0.5**	**1**	**2**	**4**	**8**
Zn-1Mg Emax (800RPM, 1:10, 1 cm, ZrO_2)	199 ± 1.5	395 ± 1.6	85.4 ± 3.0	69.3 ± 2.6	72.8 ± 3.0	82.2 ± 3.0

An important parameter of the prepared powders is the width of the particle size distribution, expressed by the span. The span of the produced alloys is given as a deviation in Tab. 2, calculated using Equation (1) and illustrated in:

$$Span = \frac{(D_{90} - D_{10})}{D_{50}} \quad (1)$$

Where:

D_{90}…Particle size below which 90% of the powder volume is present,

D_{10}…Particle size below which 10% of the powder volume is present,

D_{50}…Median particle size (mean of distribution).

The results indicate that MA produces powders with a broad particle size distribution, as a consequence of the competing processes occurring during milling. The graph (Fig. 1) shows that with increasing milling time, the distribution curve shifts towards smaller particle sizes, while simultaneously broadening, reflecting the greater spread of particle dimensions.

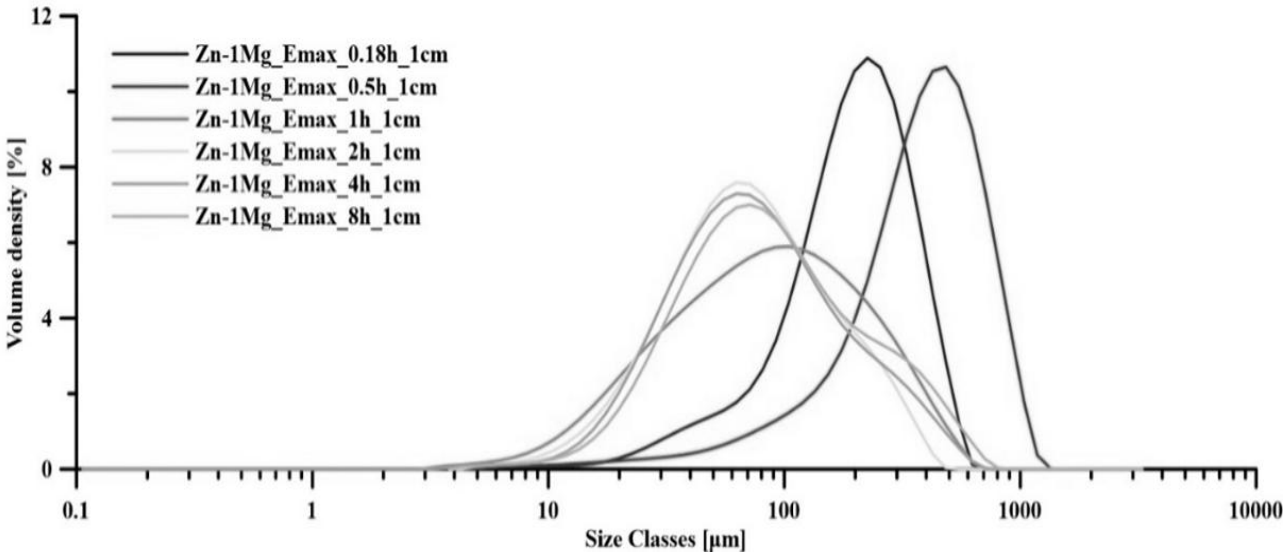

Fig. 1 *Particle size distribution of Zn-1Mg alloy prepared in Retsch Emax*

Based on these results, MA for 4 hours was selected as the best compromise between particle size distribution, phase composition, and minimal contamination from the milling equipment.

3.2 Phase composition

The results of the XRD analyses for the consolidated materials are shown in Fig. 2. The patterns obtained for both powders and compacted materials were similar, confirming that SPS is an effective method for preserving the structural characteristics developed during MA. For each alloy system, distinct localized maxima were recorded, corresponding to zinc-based secondary intermetallic phases. For the Zn–1Mg alloy, the precipitation of the Mg_2Zn_{11} intermetallic phase was identified, which is typical for this composition. Semiquantitative analysis estimated its concentration at approximately 8 wt.%. In the case of the Zn–Li alloy, MA led to the formation of an unidentified phase consistent with $ZnLi_2$. However, its concentration was very low, as indicated by weak diffraction peaks and semiquantitative calculations below 1 wt.%. This phase is not usually recorded for Zn-Li alloys with such a low concentration of alloying element. Researchers often record for alloys with a concentration below 1 wt.% of Li phase $LiZn_4$, for example, in the work of Zhao et al. [18]. Such a difference can be justified by local increases in concentration during MA. The Zn–2Mn alloy consisted of a zinc matrix and the $Zn_{13}Mn$ intermetallic phase, with an estimated concentration of about 3 wt.%. Additionally, traces of contamination (<1 wt.%) from ZrO_2 originating from the milling equipment were calculated, although no clear peaks of this phase were visible in the diffraction patterns.

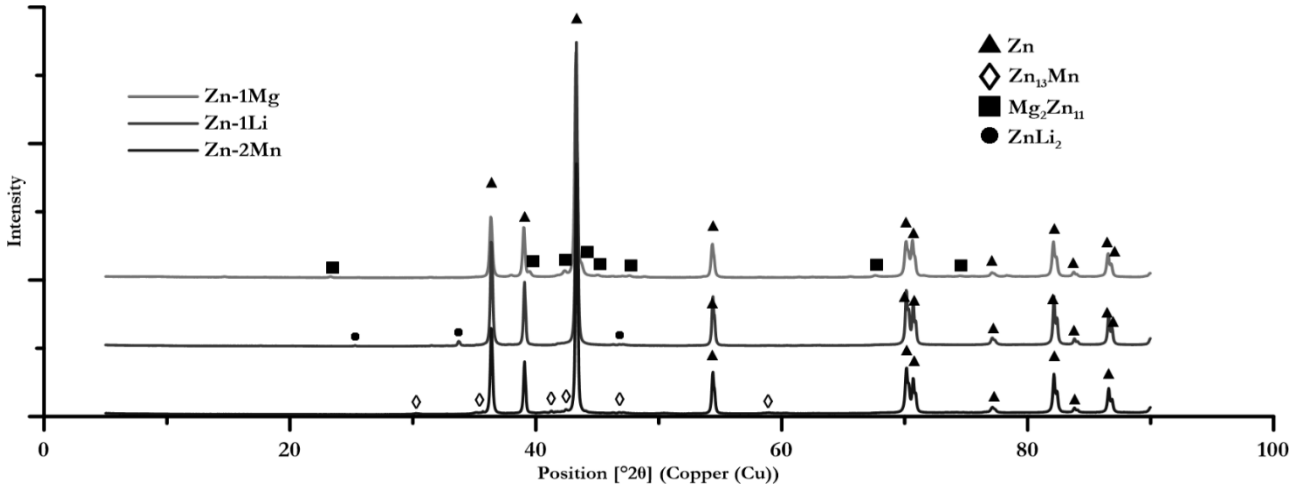

Fig. 2 *X-ray diffraction results of prepared alloys*

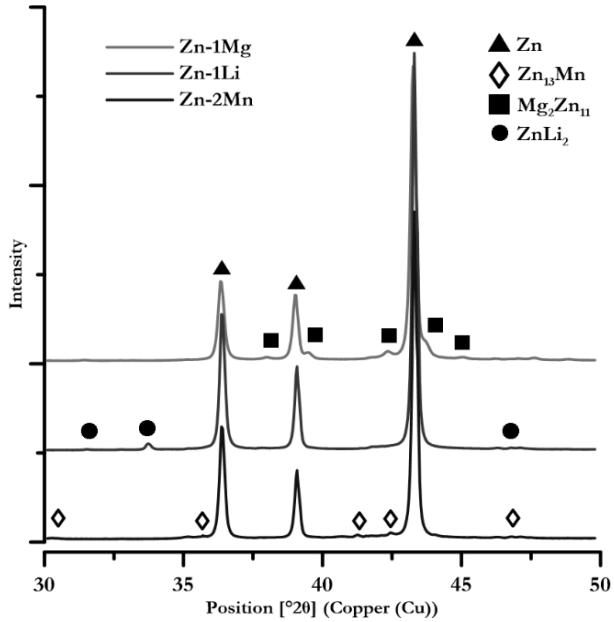

Fig. 3 *Detailed X-ray diffraction results of prepared alloys*

3.3 Microstructure of prepared materials

The microstructures of all alloys were examined using scanning electron microscopy (SEM) equipped with an EDS detector. The results, presented in Fig. 4-6, show different magnifications and the distribution of alloying elements. The lithium-based alloy was not analyzed for chemical composition due to the low atomic weight of lithium. However, the presence of lithium in the microstructure was confirmed by AAS (with the recorded value of Li 0.92 wt.%).

Fig. 4 shows the microstructure of the Zn–1Mg alloy prepared by a combination of MA and SPS. The results indicate that the selected compaction parameters were appropriate. The microstructure exhibited only a minimal amount of porosity or defects, as visible in Fig. 4A. The original surfaces of powder particles can still be observed in the form of an oxidic network structure (oxidic shells). A more detailed image in Fig. 4B reveals individual grains several micrometers in size, along with small, localized pores. These pores most likely formed during sample preparation, as less noble phases may have corroded during polishing. Grains appearing darker in contrast were identified as the Mg_2Zn_{11} intermetallic phase, as confirmed by EDS analysis. Additionally, oxygen mapping revealed elevated concentrations along the oxidic network, consistent with a ZnO and MgO mixture. Such structures are typical for materials prepared by compaction from metal powders and were recorded for zinc [19] and magnesium alloys [20-22].

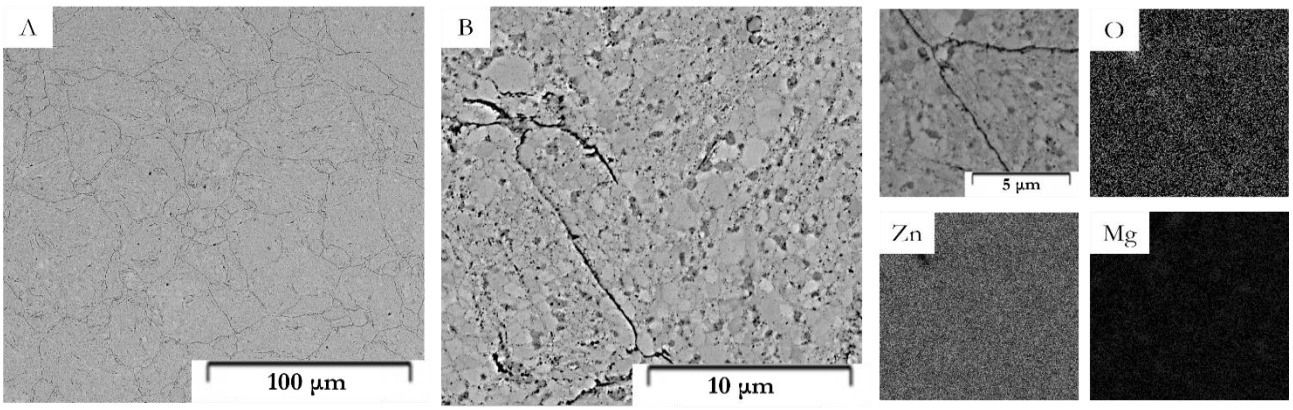

Fig. 4 *Microstructure of Zn-1Mg alloy prepared by MA and SPS (80MPa): SEM, EDS*

Fig. 5 presents the microstructure of the Zn–1Li alloy, which was consolidated under a lower pressure compared to the previous alloy. This adjustment was made due to the low melting point of lithium and its intermetallic phases, which could potentially damage the compaction equipment. Reducing the pressure resulted in a significant increase in the porosity of the material. As shown in Fig. 5A, voids are present alongside the original powder particles, delineated by oxidic shells. These voids are attributed to incomplete sintering between powder particles. A more detailed view in Fig. 5B reveals that in the consolidated sample preserved internal structure of the powder particles. A characteristic layered morphology is visible, formed by deformation during repeated particle impacts, which is a typical feature of materials prepared by MA. Small pores were also observed, most likely introduced during the sample preparation process. Additionally, locally visible small grains, several micrometers in size, were identified within the microstructure.

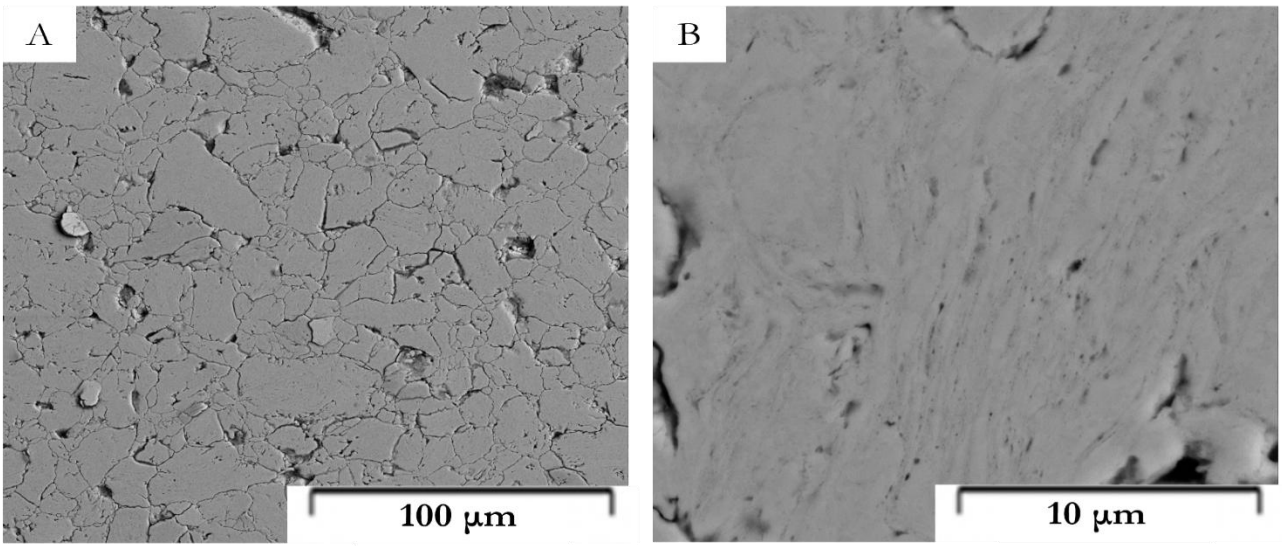

Fig. 5 *Microstructure of Zn-1Li alloy prepared by MA and SPS (40MPa): SEM*

The microstructure of the Zn–2Mn alloy is presented in Fig. 6. Among all the prepared alloy systems, this one appears the most heterogeneous. MA followed by SPS compaction produced a coarse $Zn_{13}Mn$ intermetallic phase, uniformly distributed throughout the structure in the form of rounded particles. Their distribution is clearly visible in the EDS map. In Fig. 6A, the original MA powder particles can also be seen, enclosed by oxidic shells. At higher magnification (Fig. 6B), a layered structure and very fine grains smaller than 1 μm are observed, while the grains within the intermetallic phase are coarser, reaching several micrometers. Adjacent to the intermetallic phase, a dark-grey particle was identified as ZrO_2 contamination. Localized porosity was also observed, which most probably originated from corrosion during sample preparation. A similar alloying system was also prepared by Sotoudeh Bagda et al. [23], who focused on the preparation of Zn-4Mn and Zn-24Mn (wt.%) alloy by MA. Their results also suggested precipitation of the $Zn_{13}Mn$ phase. However, the final microstructure was even more inhomogeneous, with increased porosity mainly located around the surfaces of the original particles and grains.

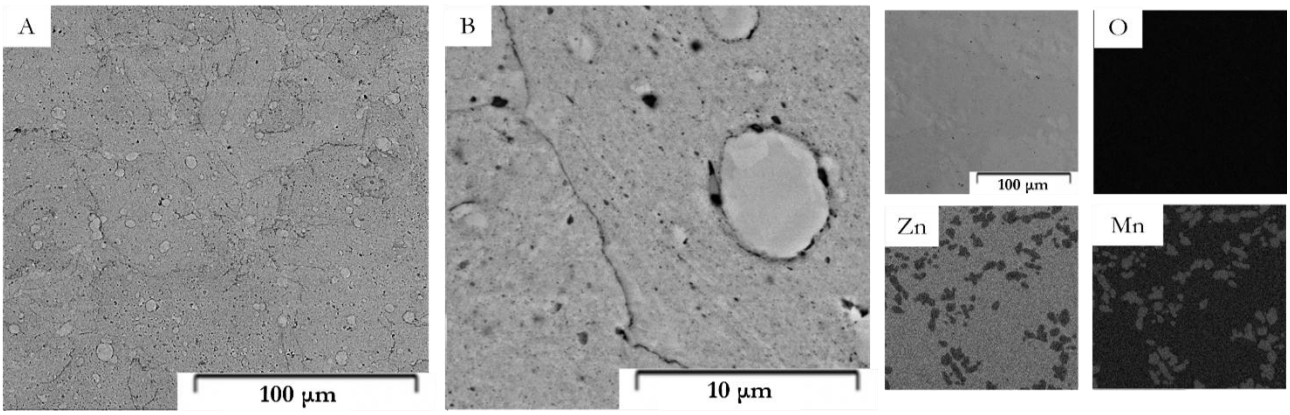

Fig. 6 *Microstructure of Zn-2Mn alloy prepared by MA and SPS (80MPa): SEM, EDS*

3.4 Mechanical properties

The mechanical properties of binary zinc-based alloys prepared by MA and SPS were evaluated by hardness and compression testing. The results are summarized in Tab. 3 and Fig. 7.

Hardness testing results (Tab. 3) highlight the critical role of secondary intermetallic phase strengthening. All prepared alloys exhibited higher hardness values compared to pure zinc, used as a reference material. The weakest strengthening effect was observed in the Zn–2Mn alloy, where the $Zn_{13}Mn$ phase formed as large particles. In contrast, the highest hardness was achieved in the Zn–1Mg alloy, where the very hard Mg_2Zn_{11} phase was present in small micrometer-sized particles.

Tab. 3 *Results of hardness and compression testing HV1*

Sample	HV1	R_p [MPa]	R_m [MPa]	A [24]
Zn-1Mg	128.0 ± 3	441.7 ± 6	526.7 ± 15	7.1 ± 1
Zn-1Li	51.0 ± 2	237.5 ± 3	-	-
Zn-2Mn	41.2 ± 1	132.7 ± 4	-	-
Zn	39.9 ± 1	134.3 ± 8	-	-

Compression testing, which provides a more comprehensive assessment than hardness, is presented in Fig. 7. The strength increase observed in the Zn–1Mg and Zn–1Li alloys correlates well with the hardness results. Both alloys outperformed pure zinc, primarily due to a combination of precipitation strengthening, solid solution strengthening, and grain refinement. In contrast, manganese addition did not improve the mechanical properties significantly.

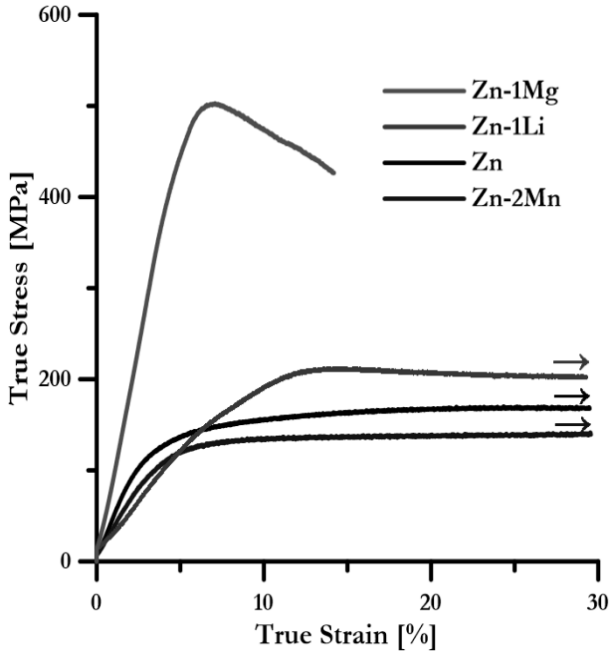

Fig. 7 *Compressive True Stress vs True Strain diagrams for studied materials*

A notable difference was observed in the stress–strain curves between Zn–1Mg and the other alloys. Pure zinc, Zn–1Li, and Zn–2Mn all showed similar plastic behavior without signs of cracking or fracture, and therefore, no distinct ultimate compressive strength was recorded. For Zn-1Li alloy, only the yield strength shifted to higher values with lithium addition, despite the lower sintering pressures used for its preparation. The Zn-2Mn alloy shows values similar to pure zinc, which suggests that precipitation of the $ZnMn_{13}$ phase had a limiting effect on strengthening. Such a low influence in strengthening was probably caused by the soft nature of $ZnMn_{13}$ (168.2 HV [11]) compared to other precipitates, such as Mg_2Zn_{11} (330 HV [25]). The Zn–1Mg alloy, however, demonstrated the highest ultimate compressive strength (526.7 MPa), attributed to the homogeneously distributed fine Mg_2Zn_{11} intermetallic particles. Nevertheless, the brittle nature of these phases reduced plasticity, which would have an even stronger effect in tests more sensitive to microstructural defects and inhomogeneities, such as tensile or bending tests.

4 Conclusion

Our results demonstrate that the combination of mechanical alloying and SPS is an effective method for achieving compact Zn–1Mg, Zn–1Li, and Zn–2Mn alloys with a fine-grained microstructure and improved mechanical properties. Even though all materials were in stable form, the Zn-1Li alloy, which was prepared by compaction at 48 MPa, showed an increased amount of porosity inside the microstructure. An increase in pressure to 80 MPa led to a significant improvement in density, which was observed for Zn-1Mg and Zn-2Mn alloy. Oxide shells were preserved in the microstructure of consolidated materials from the original surfaces of the powder precursors. Furthermore, fine intermetallic phases formed during MA remained in consolidated samples. These phases led to an improvement of compressive strength, most significantly for Zn-1Mg alloy, where the ultimate compressive strength reached up to 526.7 MPa. However, precipitation of phases led to a significant reduction of plasticity. The best combination of strength and plasticity was achieved for Zn-1Li alloy.

Data availability

The data mentioned in the present manuscript are accessible via the Zenodo repository: https://doi.org/10.5281/zenodo.17640120.

Acknowledgement

This research was supported by the Czech Science Foundation (project no. 25-16144S), Specific University research (project no. A1_FCHT_2025_011), and by the project "Mechanical Engineering of Biological and Bio-inspired Systems", funded as project No. CZ.02.01.01/00/22_008/0004634 by Programme Johannes Amos Commenius.

References

[1] KUBÁSEK, J., DVORSKÝ, D., ČAPEK, J., MARKÉTA, S., KLÁRA, H., & VOJTĚCH, D. (2020). Zinc alloys as prospective materials for biodegradable medical devices. In: *Manufacturing Technology*, Vol. 20, No. 6, pp. 779-784. DOI: 10.21062/mft.2020.113.

[2] KUBASEK, J., & VOJTĚCH, D. (2012). Zn-based alloys as an alternative biodegradable materials. In: *Proc. Metal*, Vol. 5, No. 23-25.

[3] VOJTECH, D., KUBASEK, J., SERAK, J., & NOVAK, P. (2011). Mechanical and corrosion properties of newly developed biodegradable Zn-based alloys for bone fixation. In: *Acta Biomater*, Vol. 7, No. 9, pp. 3515-22. DOI: 10.1016/j.actbio.2011.05.008.

[4] FARMANI, A.R., SALMEH, M.A., GOLKAR, Z., MOEINZADEH, A., GHIASI, F.F., AMIRABAD, S.Z., SHOORMEIJ, M.H., MAHDAVINEZHAD, F., MOMENI, S., MORADBEYGI, F., AI, J., HARDY, J.G., & MOSTAFAEI, A. (2022). Li-Doped Bioactive Ceramics: Promising Biomaterials for Tissue Engineering and Regenerative Medicine. In: *Journal of Functional Biomaterials*, Vol. 13, No. 4, pp. 162.

[5] ARAL, H., & VECCHIO-SADUS, A. (2008). Toxicity of lithium to humans and the environment--a literature review. In: *Ecotoxicol Environ Saf*, Vol. 70, No. 3, pp. 349-56. DOI: 10.1016/j.ecoenv.2008.02.026.

[6] HAUSSLER, J., & BADER, M. (2015). An interference account of the missing-VP effect. In: *Front Psychol*, Vol. 6, No. 766. DOI: 10.3389/fpsyg.2015.00766.

[7] SHI, Z.-Z., YU, J., & LIU, X.-F. (2018). Micro-alloyed Zn-Mn alloys: From extremely brittle to extraordinarily ductile at room temperature. In: *Materials & Design*, Vol. 144, No. 343-352. DOI: https://doi.org/10.1016/j.matdes.2018.02.049.

[8] MOSTAED, E., SIKORA-JASINSKA, M., DRELICH, J.W., & VEDANI, M. (2018). Zinc-based alloys for degradable vascular stent applications. In: *Acta Biomaterialia*, Vol. 71, No. 1-23. DOI: https://doi.org/10.1016/j.actbio.2018.03.005.

[9] KAMMERER, C.C., BEHDAD, S., ZHOU, L., BETANCOR, F., GONZALEZ, M., BOESL, B., & SOHN, Y.H. (2015). Diffusion kinetics, mechanical properties, and crystallographic characterization of intermetallic compounds in the Mg–Zn binary system. In: *Intermetallics*, Vol. 67, No. 145-155. DOI: https://doi.org/10.1016/j.intermet.2015.08.001.

[10] REN, T., GAO, X., XU, C., YANG, L., GUO, P., LIU, H., CHEN, Y., SUN, W., & SONG, Z. (2019). Evaluation of as-extruded ternary Zn–Mg–Zr alloys for biomedical implantation material: In vitro and in vivo behavior. In: *Materials and Corrosion*, Vol. 70, No. 6, pp. 1056-1070. DOI: https://doi.org/10.1002/maco.201810648.

[11] SHI, Z.Z., GAO, X.X., ZHANG, H.J., LIU, X.F., LI, H.Y., ZHOU, C., YIN, Y.X., & WANG, L.N. (2020). Design biodegradable Zn alloys: Second phases and their significant influences on alloy properties. In: *Bioact Mater*, Vol. 5, No. 2, pp. 210-218. DOI: 10.1016/j.bioactmat.2020.02.010.

[12] KRATOCHVÍL, P., & PRŮŠA, F. (2022). CoCrFeNiTi High Entropy Alloy Prepared via Mechanical Alloying and Spark Plasma Sintering. In: *Manufacturing Technology Journal*, Vol. 22, No. 4, pp. 423-428. DOI: 10.21062/mft.2022.049.

[13] THÜRLOVÁ, H., & PRŮŠA, F. (2022). Partial Substitution of Mn by Al in the Cocrfenimnxal20-X (X=5, 10, 15) High Entropy Alloy Prepared of Mechanical Alloying and Spark Plasma Sintering. In: *Manufacturing Technology Journal*, Vol. 22, No. 3, pp. 342-346. DOI: 10.21062/mft.2022.045.

[14] SURYANARAYANA, C. (2001). Mechanical alloying and milling. In: *Progress in Materials Science*, Vol. 46, No. 1, pp. 1-184. DOI: https://doi.org/10.1016/S0079-6425(99)00010-9.

[15] SURYANARAYANA, C. (2019). Mechanical Alloying: A Novel Technique to Synthesize Advanced Materials. In: *Research (Wash D C)*, Vol. 2019, No. 4219812. DOI: 10.34133/2019/4219812.

[16] NEČAS, D., HYBÁŠEK, V., PINC, J., ŠKOLÁKOVÁ, A., VOŇAVKOVÁ, I.,

HOSOVÁ, K., ZLÁMAL, M., BOUKALOVÁ, A., POKORNÝ, J., DVORSKÝ, D., MINÁRIK, P., VESELÝ, J., DONIK, Č., VOJTĚCH, D., & KUBÁSEK, J. (2024). Exploring the microstructure, mechanical properties, and corrosion resistance of innovative bioabsorbable Zn-Mg-(Si) alloys fabricated via powder metallurgy techniques. In: *Journal of Materials Research and Technology*, Vol. 29, No. 3626-3641. DOI: https://doi.org/10.1016/j.jmrt.2024.02.066.

[17] NECAS, D., MAREK, I., PINC, J., VOJTECH, D., & KUBASEK, J. (2022). Advanced Zinc-Magnesium Alloys Prepared by Mechanical Alloying and Spark Plasma Sintering. In: *Materials (Basel)*, Vol. 15, No. 15, pp. DOI: 10.3390/ma15155272.

[18] ZHAO, S., SEITZ, J.-M., EIFLER, R., MAIER, H.J., GUILLORY, R.J., EARLEY, E.J., DRELICH, A., GOLDMAN, J., & DRELICH, J.W. (2017). Zn-Li alloy after extrusion and drawing: Structural, mechanical characterization, and biodegradation in abdominal aorta of rat. In: *Materials Science and Engineering: C*, Vol. 76, No. 301-312. DOI: https://doi.org/10.1016/j.msec.2017.02.167.

[19] NEČAS, D., KUBÁSEK, J., PINC, J., MAREK, I., DONIK, Č., PAULIN, I., & VOJTĚCH, D., (2022). Ultrafine-Grained Zn-Mg-Sr Alloy Synthesized by Mechanical Alloying and Spark Plasma Sintering. *Materials*, 15, DOI: 10.3390/ma15238379.

[20] DVORSKY, D., KUBASEK, J., & VOJTECH, D. (2017). Corrosion protection of WE43 magnesium alloy by fluoride conversion coating. In: *Manufacturing Technology*, Vol. 17, No. 4, pp. 440-446.

[21] DVORSKÝ, D., KUBÁSEK, J., KRISTIANOVÁ, E., & VOJTĚCH, D. (2018). Corrosion resistant magnesium-based composite material with MgF2 continuous network prepared by powder metallurgy. In: *Manufacturing Technology*, Vol. 18, No. 5, pp. 737-741. DOI: 10.21062/ujep/180.2018/a/1213-2489/MT/18/5/737.

[22] DVORSKY, D., KUBASEK, J., & VOJTECH, D. (2018). A new approach in the preparation of biodegradable Mg-MgF2 composites with tailored corrosion and mechanical properties by powder metallurgy. In: *Materials Letters*, Vol. 227, No. 78-81. DOI: https://doi.org/10.1016/j.matlet.2018.05.052.

[23] SOTOUDEH BAGHA, P., KHALEGHPANAH, S., SHEIBANI, S., KHAKBIZ, M., & ZAKERI, A. (2018). Characterization of nanostructured biodegradable Zn-Mn alloy synthesized by mechanical alloying. In: *Journal of Alloys and Compounds*, Vol. 735, No. 1319-1327. DOI: 10.1016/j.jallcom.2017.11.155.

[24] PINC, J., MIKLÁŠOVÁ, E., PRŮŠA, F., ČAPEK, J., DRAHOKOUPIL, J., & VOJTĚCH, D.J.M.T. (2019). Influence of processing on the microstructure and the mechanical properties of Zn/HA8 wt.% biodegradable composite. In: *Manufacturing Technology*, Vol. 19, pp. 836-841.

[25] HERNÁNDEZ-ESCOBAR, D., CHAMPAGNE, S., YILMAZER, H., DIKICI, B., BOEHLERT, C.J., & HERMAWAN, H. (2019). Current status and perspectives of zinc-based absorbable alloys for biomedical applications. In: *Acta Biomaterialia*, Vol. 97, No. 1-22. DOI: https://doi.org/10.1016/j.actbio.2019.07.034.